Natural Hazards
and Earth System
Sciences

Open Access

On precipitation measurements collected by a weather radar and a rain gauge network

S. Sebastianelli[1,2]**, F. Russo**[1]**, F. Napolitano**[1]**, and L. Baldini**[2]

[1]Dipartimento di Ingegneria Civile, Edile e Ambientale, Sapienza Università di Roma, Rome, Italy
[2]National Research Council, Institute of Atmospheric Sciences and Climate, Rome, Italy

Correspondence to: F. Russo (fabio.russo@uniroma1.it)

Abstract. Many phenomena (such as attenuation and range degradation) can influence the accuracy of rainfall radar estimates. They introduce errors that increase as the distance from radar increases, thereby decreasing the reliability of radar estimates for applications that require quantitative precipitation estimation. The present paper evaluates radar error as a function of the range, in order to correct the rainfall radar estimates. The radar is calibrated utilizing data from the rain gauges. Then, the G/R ratio between the yearly rainfall amount measured in each rain gauge position during 2008 and the corresponding radar rainfall amount is calculated against the slant range. The trend of the G/R ratio shows two behaviours: a concave part due to the melting layer effect close to the radar location and an almost linear, increasing trend at greater distances. A best fitting line is used to find an adjustment factor, which estimates the radar error at a given range. The effectiveness of the methodology is verified by comparing pairs of rainfall time series that are observed simultaneously by collocated rain gauges and radar. Furthermore, the variability of the adjustment factor is investigated at the scale of event, both for convective and stratiform events. The main result is that there is not a univocal range error pattern, as it also depends on the characteristics of the considered event. On the other hand, the adjustment factor tends to stabilize itself for time aggregations of the order of one year or greater.

1 Introduction

Weather radar is able to provide, in real time and over a wide region, high spatial- and temporal-resolution rainfall intensity estimates. Therefore, it plays a significant role in the rainfall field estimation and consequently in the improvements of hydrograph simulation, which is necessary for providing flood forecasting and forewarning (with a safety margin) and for the design of drainage systems (Clothier and Pegram, 2002).

Weather radar has been established as an invaluable tool for the provision of weather services, as it facilitates monitoring of precipitation events and predicts their short time evolution. However, it is not as well established as a tool for the quantitative estimation of precipitation (Delrieu et al., 2009). Thus, for many applications (especially those requiring long-term precipitation estimates, such as those related to hydraulic risk assessment) conventional measurements from a network of sparse rain gauges are still preferred. In fact, when comparing data from rain gauges with the corresponding radar estimates, errors are found that depend on the distance of rain gauges with respect to the radar position. Many sources of error affect radar rainfall estimates at the ground level: these include radar miscalibration, range degradation (including beam broadening and sampling of precipitation at increasing altitude), path attenuation, ground clutter, instrument sensitivity, vertical variability of the precipitation system, vertical air motion, precipitation drift, temporal sampling error, anomalous propagation, beam-filling effects and beam blocking (Brandes et al., 1999; Villarini and Krajewski, 2010). These produce an overall error, which tends to increase as the distance from radar increases. As a

consequence, the spatial structure of a rain field that is derived from weather radar measurements that are collected at low (but not null) elevation angles is affected by the way that the radar samples precipitation and is therefore dependent both on the height and size of the radar's sample volume (which increase as the distance from radar increases) and on orography (the latter influences errors due to ground clutter and beam blocking).

As noted above, the accuracy of radar estimates has been traditionally assessed by performing a comparison with rainfall measurements at ground obtained by rain gauges. Factors producing discrepancies between radar and rain gauge data can produce the following errors (Zawadzki, 1984): (1) random errors, such as the error associated with the transformation from reflectivity to rain rate due to the variability of drop size distribution (DSD); (2) systematic errors (Villarini et al., 2008b) due to radar miscalibration; (3) range-dependent errors, such as the sampling uncertainties that are associated with the beam broadening and the increase in height with range of the sample volume (Berenguer and Zawadzki, 2008; Berenguer and Zawadzki, 2009), which cause temporal and spatial sampling differences of the two devices (Villarini et al., 2008a).

Radar reflectivity factor (Z) and rainfall intensity (R) both depend on the hydrometeor water-phase distribution within the sampled volume. Saltikoff et al. (2000) apply (individually at each radar pixel and in real time) an optimal relation between the reflectivity factor and the precipitation intensity, by using water-phase-adjusted radar data. They then compare the values of accumulated precipitation obtained from both rain gauge and radar data.

Giangrande and Ryzhkov (2003, 2005) and Wang and Chandrasekar (2010) demonstrate (at S- and X-band respectively) a statistical improvement in radar rainfall quantitative estimates by utilizing polarimetric algorithms based on the specific differential phase $K_{DP} - R$ instead of the $Z - R$ conventional algorithm. In fact, the specific differential phase is immune to radar miscalibration, path attenuation, and partial beam blocking and is less sensitive to DSD variability, but measurement error is quite high especially for light precipitation (Vulpiani et al., 2012). To provide precipitation estimates at long ranges Giangrande and Ryzhkov (2008) investigate the quality of polarimetric rainfall estimation at far distances from an S-band polarimetric weather radar. Recently, to overcome error due to range degradation and attenuation, a low-power, short-range, dense radar network has been used. In particular, the dense network approach allows the radars that comprise a network to sample at low altitude, with higher spatial resolution and increased sensitivity. Moreover, the different radar measures available can be combined to estimate the path attenuation (Junyent and Chandrasekar, 2009).

The ratio between rain gauge readings and the corresponding radar estimates has been often employed to correct the mean field bias due to uncertainties in $Z - R$ relationship and system non-optimal calibration (Seo et al., 2000; Borga and Tonelli, 2000; Gjertsen et al., 2004; Krajewski et al., 2011). However, the use of this technique is reasonable only at short ranges, where the effects of range degradation are negligible and the G/R ratio is relatively low and constant, or if a dense rain gauge network is available in the radar domain.

$Z-R$ relation coefficients depend on the DSD and, therefore, vary in time and space, as well as the $Z-R$ relation varying geographically depending on the type of precipitation (Koistinen and Puhakka, 1986; Saltikoff et al., 2000; Villarini and Krajewski, 2010). On the other hand, rain fields observed by Polar 55C in the cold season are usually composed of cores of convection embedded in larger stratiform precipitation regions, as is largely confirmed in the literature (Houze, 1997; Vignal et al., 2000; Zhang et al., 2008; Zhang and Qi, 2010). Thus, the error introduced by the $Z-R$ relationship is a random error which varies in space. Therefore, we estimate an invariant with space multiplicative bias M only to correct systematic error due to radar miscalibration. Moreover, rain gauge data utilized for this issue are collected only at short ranges, as better detailed in Sect. 4.

A further consequence is that comparison between rain gauge and radar rains at the same location depends on the selected $Z-R$ relationship (Koistinen and Puhakka, 1986).

If the G/R ratio varies too rapidly with distance, the mean field bias adjustment method must be coupled with a procedure for removing range-dependent bias due to non-uniform vertical profile of reflectivity (VPR). The literature offers a number of procedures for real-time adjustment of range-dependent biases (Seo et al., 2000; Borga and Tonelli, 2000; Vignal et al., 2000; Vignal et Krajewski, 2001; Gjertsen et al., 2004; Zhang et al., 2008; Zhang and Qi, 2010; Krajewski et al., 2011).

In this paper we identify an approach to the assessment of overall range-dependent error. Range-dependent error occurs as a result of various sources of uncertainty, such as range degradations, attenuation, radar sampling within the melting layer, and vertical variability of precipitation. The range error can be expressed as a function of the slant range through an adjustment factor (AF). This is used as a range error pattern, allowing the mean error that influences long-term quantitative precipitation estimates (QPE) to be corrected. In order to achieve this, a comparison is made between radar estimates and rain gauge measurements at different distances from radar, based on the assumption that the gauge represents the truth, being a direct measurement of rainfall accumulation. This implies that we are neglecting the area-point error introduced when the radar areal information is compared with gauge point measurement. Although this hypothesis is simplistic, it is true that error in rain gauge estimation does not depend on the distance from the radar. A range-dependent gauge adjustment technique (Michelson and Koistinen, 2000) is applied in combination with a radar calibration that is based on data from the rain gauges (the latter is performed prior to AF estimation). Issues like attenuation, VPR-related error, bright band, and incorrect $Z-R$

relationship are implicitly treated with this type of method (Gjertsen et al., 2004). Errors arising from orography are not considered.

The correspondence between pairs of rainfall processes observed simultaneously by radar and by each rain gauge at the rain gauge position is investigated through the analysis of trend with range of the fractional standard error (FSE) index, slope of the scatter plots' regression lines between G and R and the G/R ratio between rain gauges' and radar rainfall amounts.

Rainfall intensity maps, derived from reflectivity measurements collected with the Polar 55C weather radar in 2008 and 2009, are utilized. Radar calibration is performed by using only 2008 radar and rain gauge data sets, as well as the AF estimate. Finally, to verify the effectiveness of the methodology, the synthetic index, the slope of the scatter plots' regression lines and the G/R ratio behaviours are analysed as a function of the range, for both the 2008 data sets and for 2009 data sets.

The paper is organized as follows. In the next section, the characteristics of Polar 55C weather radar are described. In Sect. 3 the methodology followed for data selection is detailed. In Sect. 4 the radar calibration method is explained. In Sect. 5 the adjustment factor is defined. In Sect. 6 the AF variability is discussed. In Sect. 7 the adjustment procedure is verified, and, finally, Sect. 8 completes the paper with conclusions.

2 Processing of radar data

2.1 The Polar 55C weather radar

The Polar 55C is a C-band (5.6-GHz) Doppler dual polarized coherent weather radar with polarization agility managed by the CNR-ISAC (Institute of Atmospheric Sciences and Climate of the National Research Council) in Italy. The radar is located 15 km south-east of Rome (lat. 41.84° N, long. 12.65° E, 102 m above sea level). The receiver/transmitter apparatus is a fully coherent one. In particular, the transmitter is based on a klystron amplifier which allows for very high pulse-to-pulse and phase stability. The klystron uses a nominal peak power of 250 kW. In the considered data sets, radar measurements are obtained by averaging from 48 to 64 pulses transmitted with a 1200-Hz pulse repetition frequency in range bins spaced 75 m apart. Data are collected up to 120 km away from the radar location. The antenna geometry is a single off-set type to avoid beam blocking by stalls which could both increase the cross-polarization level and cause differences in radiation patterns in H and V polarizations. Half-power beams are 0.92° and 1.02° in azimuth and elevation, respectively. The antenna is not protected by a radome. The digital radar signal processor can exploit the sampling of the transmitted waveform, in order to perform a pulse by pulse calibration (Gorgucci et al., 2002). Since

Polar 55C is not an operational weather radar, different scanning strategies are adopted. Each scanning strategy includes a 1.5° nominal elevation, which is considered in this study for long-term QPE because this angle minimizes the influence of ground-clutter and meets the requirement to keep the radar beam close to the ground (Gorgucci et al., 1995; Russo et al., 2005, 2006; Lombardo et al., 2006a). All the case studies of the collected data sets contain a sweep at 1.5° elevation collected with a repetition time of five minutes. However, in order to investigate the variability of the AF at the scale of event we consider different elevation angles ranging from 1.5 to 5.5° (see Sect. 5).

2.2 From reflectivity data to rainfall intensity maps

Polar 55C radar data are collected without filtering out noise. In order to define a threshold for the signal-to-noise ratio, we suppose that, at great distances, the Polar 55C, also with relatively low elevations (for example, 1.5°), will likely sample in an atmospheric region above the precipitation. This is likely to happen in stratiform precipitation, but not with convective cells. On the other hand, convective precipitation cells are not very widespread in space. For this reason, for each sweep, the last two range bins of each record are identified and the modal value of reflectivity measured in these 720 range bins (i.e. 360 radials × 2 range bins) is used as a proxy of the noise power measured by the receiver. The use of a modal value allows the neglection of the possible presence of reflectivity of convective cells at far distances which likely affect a few radials. The noise level Z_N in dBZ at a given range r can be expressed by Eq. (1) as follows:

$$Z_N(r) = pZ_f + 20\log_{10}(r/r_{end}), \tag{1}$$

where in the second term in the right side r_{end} is the maximum range and Z_f is the modal value (determined as described previously) at the farther two range bins. Therefore, Z_f refers only to a single sweep, and Z_N does not depend on the azimuth, but it is a function only of the range. Along a ray, each measured Z_h value at the distance r is compared with the Z_N value at the same distance, and the range bins whose reflectivity does not exceed the noise level by a threshold of 4 dB are considered as being affected by noise. This method allows both monitoring of the noise level of the system and identifying returns with a signal-to-noise ratio above a given threshold (in dB). An advantage of the method is that it does not require accurate modelling of noise (Peebles, 1998) or measurements of parameters predicting system noise power. The method developed to identify and remove range bins affected by ground clutter is based on the existence of typical values for the standard deviations of the differential reflectivity and of the differential phase when the radar return is caused by precipitation (Bringi and Chandrasekar, 2001). Standard deviations are computed using a moving window along each radar ray of 5 range bins, as described also in Lombardo et al. (2006b). Used thresholds for

clutter identifications are:

$$0.09\,\mathrm{dB} < \sigma\,(Z_{\mathrm{DR}}) < 0.9\,\mathrm{dB} \qquad (2)$$
$$\sigma\,(\Phi_{\mathrm{DP}}) < 5°.$$

The reflectivity data of Polar 55C are corrected for the calibration bias by adding a correction factor C to each recorded Z_{h} value. C is obtained by performing a calibration with rain gauges (Koistinen and Puhakka, 1986; Saltikoff et al., 2000), as explained in Sect. 4.

Only the radar reflectivity that corresponds to meteorological returns is converted into rainfall intensity by using the parametric algorithm (Gorgucci and Baldini, 2009):

$$R = 0.19055 \cdot 10^{(0.5358(Z_{\mathrm{h}}/))}, \qquad (3)$$

where Z_{h} is the reflectivity factor at horizontal polarization (dBZ) and R is the rainfall intensity (in $\mathrm{mm\,h^{-1}}$). Coefficients of this algorithm are determined through **T** matrix simulations (Barber and Yeh, 1975), assuming a theoretically derived distribution of the DSD parameters, the drop shape model of Pruppacher and Beard (1970), a fixed temperature of $20\,°\mathrm{C}$ and a Gaussian distribution of canting angle with 0 mean and standard deviation at 10 degrees (Bringi and Chandrasekar, 2001, Sect. 8.1).

Finally, radar rainfall intensity maps are obtained by remapping radar polar range bins onto a 1-km^2 Cartesian grid. A radar rainfall map consists of 240×240 rain rate values ($\mathrm{mm\,h^{-1}}$), each of which pertains to one of the pixels of the Cartesian grid. A pixel is a square with 1-km sides. However, radar obtains a reflectivity value for each sample volume (range bin) that has a fixed length of 75 m, but both width and thickness depend on the distance. Thus, the number of range bins within each 1-km^2 pixel varies with distance. Rain rate in pixel is determined by calculating the average of the rain values of the range bins including inside it. The computation of the mean value does not take into account the range bins affected by ground clutter or noise.

3 Data

3.1 Radar data

The analysis takes into account 148 rainfall events which occurred during 2008 and 2009. Pairs of rainfall time series are observed by Polar 55C as well as at each rain gauge position during each of these events.

Zero rainfall values can be found in the time series of both the radar and the rain gauges. Yoo and Ha (2007) and Ha and Yoo (2007) have shown that zero measurements cannot be used for characterizing a rainfall field from rain gauge measurements because they decrease the spatial variability of the data and produce a high variability of the correlation between pairs of time series, with several abnormally high estimates. However, considering pairs of radar and gauge rainfall series, zero radar rainfall estimates occur especially at far ranges,

when the radar returns from precipitation can be quite close to the minimum detectable signal due to range degradation or attenuation. On the other hand, if there are no rainy areas smaller than a radar pixel, it is possible that a rain gauge included in that pixel does not detect rainfall, even though the relative radar rainfall value is greater than zero (Villarini et al., 2008a). Moreover, during the warm season, when convective events occur, rain gauges could not detect rainfall, depending on the non-uniform density of the rain gauge network and on the small extension of precipitation areas (Maheepala et al., 2001). Therefore, homologues pairs with at least an intensity value different from zero, in corresponding radar and rain gauge time series, are useful for highlighting the differences between radar estimates and rain gauge measurements. For this reason, they have been also considered to characterize radar error against range.

3.2 Rain gauge data

Radar rainfall estimates are compared with the rain measured by a set of 40 tipping bucket rain gauges managed by Regione Lazio – Ufficio Idrografico e Mareografico and located inside the radar scanning area. Gauge rain is compared with that of the radar pixels that contain it. Rain gauges are equipped with individual small dataloggers that can record the bucket tip times. The bucket makes an electrical contact during the tip, so that, each time it tips, an electronic signal is recorded to a datalogger. These records are downloaded to a personal computer via standard serial interface. Then, they are validated through a double mass analysis to check their consistency by Regione Lazio – Ufficio Idrografico e Mareografico. Rain gauges have time resolutions of 10 or 15 min and a rain resolution of 0.2 mm h^{-1}. Before comparison, the rainfall amounts of radar and rain gauges are calculated by considering an accumulation time ranging from 30 to 90 min, to overcome the problem due to the rain gauges' sampling delay with regard to the radar.

Only the rain gauges located in sectors with good radar visibility are considered, to avoid cases of partial or total beam blocking, which would invalidate locally the radar error trend with range estimation. This is done by estimating the radar visibility using the digital elevation model (DEM) with a resolution of 800 m × 600 m, produced by the Servizio Geologico Nazionale. Figure 1 shows the case-study region and the positions of the rain gauges with respect to the Polar 55C location.

4 Weather radar calibration with rain gauges

To calibrate the Polar 55C, a comparison is made between radar and rain gauges' rainfall amounts, using the 2008 rain gauge data set. However, only six rain gauges are chosen (see Fig. 2) to calculate bias (namely Ostiense, Acqua Acetosa, Cassiodoro, Roma Sud, Roma Nord, and Monte Mario), so
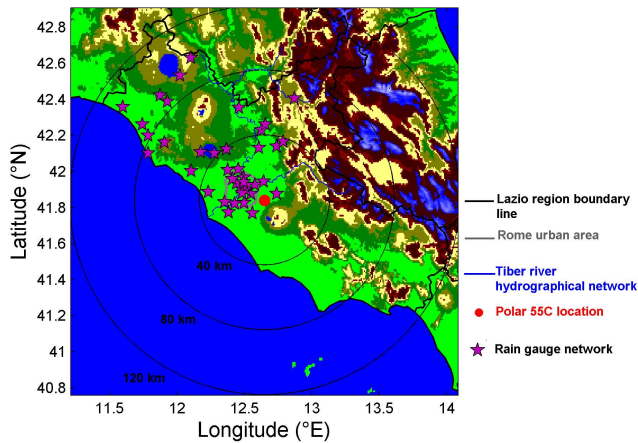
Fig. 1. Test area and rain gauge positions. Also shown are Polar 55C location, the Rome urban area and the hydrographical network of the Tiber River. Range rings are centred on Polar 55C.
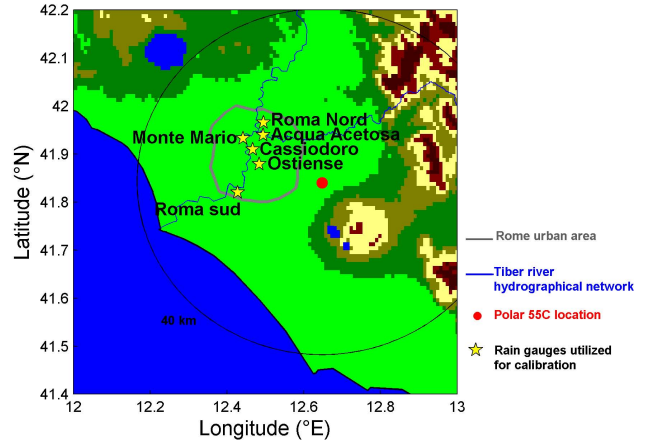

Fig. 2. Locations of rain gauges utilized to perform Polar 55C calibration.

that radar errors at the sites of the rain gauges can only be attributed to radar miscalibration, avoiding the influence of the other kinds of radar errors on bias calculation. Accordingly, only rain gauges located in areas with good radar visibility are chosen to avoid errors due to partial or total beam blocking. Moreover, rain gauges are chosen in a range from 15 to 20 km to minimize range degradation effects or errors due to attenuation (because of the short paths) and antenna side lobe effects (urban clutter), the latter avoiding short ranges. So as it is calculated, it is an average bias within the range of distances in which the rain gauges are chosen.

A multiplicative error M is obtained as follows:

$$M = \frac{\sum\limits_{i=1}^{E} \sum\limits_{j=1}^{P} G_{i,j}}{\sum\limits_{i=1}^{E} \sum\limits_{j=1}^{P} R_{i,j}} \qquad (4)$$

where $G_{i,j}$ and $R_{i,j}$ are the rain gauges' and the radar rainfall amount, respectively, for i-th event and j-th rain gauge; E is the number of rainfall events observed during 2008; and P is the number of selected rain gauges. M is utilized to calculate radar bias C in dB as follows:

$$C = \frac{10}{b} \log_{10}(M), \qquad (5)$$

where b is the same exponent of Eq. (3) and its value is 0.5358. C is a factor that must be added to reflectivity data to correct the effects of radar miscalibration and that is the same as multiplying radar rain by M. The resulting value of C is -8.62.

Figure 3 shows the trend of the Kendall correlation coefficient as a function of the slant range, obtained between 40 pairs of rain series collected by Polar 55C and by each rain gauge considered, including those utilized for calibration. In
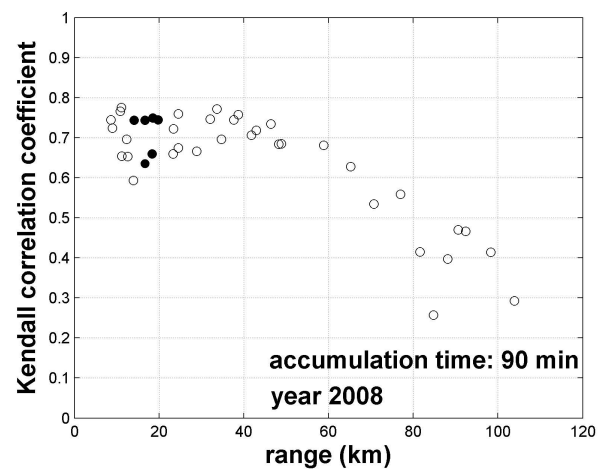

Fig. 3. Trend against range of the Kendall coefficient before radar calibration (with an accumulation time of 90 min) performed by using 2008 data. Black dots refer to the rain gauges chosen for radar calibration.

the absence of range degradation or attenuation effects, high correlation between rainfall radar estimates and rain gauge measurements is expected. In fact, the black dots in Fig. 3 (rain gauges selected for calibration) show among the highest correlation between pairs of rainfall processes observed by the two devices. This correlation trend concerns an accumulation time of 90 min. Since rainfall data are skewed, the Pearson correlation coefficient estimates, usually computed to investigate the relationships between pairs of rainfall time series referring to different locations, may exhibit bias and high variance. For this reason, as proposed by Serinaldi (2008), the Kendall correlation coefficient is utilized here (Kendall, 1949; Kendall and Stuart, 1973; Habib et al., 2001). Moreover, it must be noted that correlation coefficient value is independent from bias calibration; i.e. correlation

coefficient remains the same by performing an increasing linear transformation of one or both of the variables.

5 Adjustment Factor estimate

In the presence of range-dependent errors, also an adjustment factor depending on the range must be added to reflectivity data. As well as the overall average bias calculation, the isotropic range dependent bias, AF, is estimated by using only the radar data set collected in 2008. Once the Polar 55C calibration has been performed, the G/R ratio between the rainfall amount at each gauge site (G) and the respective radar rainfall amount (R) is computed. Data observed during 2008 are used to estimate the G/R ratios: in fact the G/R ratio becomes more stable for longer accumulation times, because the influence of uncertainty caused by mismatches in time and space performed by the two devices is reduced (Gabella and Amitai, 2000; Gabella et al., 2001; Gjertsen et al., 2004; Ozturk and Yilmazer, 2007). A vector of G/R ratios is created, which has as many elements as the number of rain gauges utilized (40). Each component of the vector is defined as follows:

$$\left(\frac{G}{R}\right)_j = \frac{\sum\limits_{i=1}^{E} G_i}{\sum\limits_{i=1}^{E} R_i} \quad j = 1, 2, \ldots, 40, \tag{6}$$

where G_i and R_i are the rain gauge and the radar rainfall amounts for the i-th event, respectively; E is the number of rainfall events observed during 2008; and the subscript j refers to a specific rain gauge.

Since rain gauges are located at different distances from Polar 55C, the trend of the logarithm of G/R as a function of the range is subsequently evaluated, and two different behaviours are found depending on the distance. Figure 4 shows a comparison between $\log(G/R)$ obtained before (row data) and after the radar calibration. Within the range of about 50 km the behaviour of $\log(G/R)$ is influenced by the presence of the bright band, which causes a radar overestimation of rain, as better detailed in Sect. 7. However, at the same time, the effects of attenuation and range degradation are reduced – the latter due to the fact that at an elevation of 1.5 degrees the 1-degree beam of Polar 55C samples precipitation sufficiently close to the ground (in fact, at an elevation of 1.5°, at a distance of 50 km the height of the centre of the radar beam is situated at an altitude of about 1.5 km above the ground). But, beyond this range, an almost-increasing linear trend of the logarithm of the G/R ratios occurs (up to a value of 2 after radar calibration), and this means that radar error increases with range, indicating an increasing radar underestimation of rainfall as a function of the range. As a consequence, radar estimates need to be corrected through a proper AF. Therefore, after calculating the logarithm of G/R as a
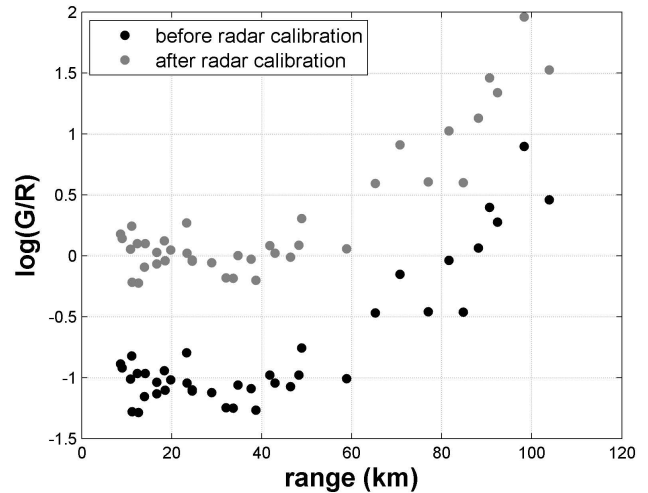

Fig. 4. G/R trend with distance from Polar 55C. Rain gauge data and radar data collected during 2008. Black dots refer to the initial radar data set, while grey dots reflect data that are obtained after radar calibration with a subset of rain gauges.

function of range, the best fitting line shown in the left plot of Fig. 5 is used to find the AF (dB) by applying the following empirical relation:

$$\text{AF}(r) = \frac{10}{b} \log_{10}(e^X), \tag{7}$$

where X is the regression model of the logarithm of G/R, given by Eq. (8):

$$X = p_1 r^5 + p_2 r^4 + p_3 r^3 + p_4 r^2 + p_5 r + p_6 \tag{8}$$

and p_1, p_2, p_3, p_4, p_5, and p_6 are the coefficients of the best fitting line, r is the range and b has the same value as in Eq. (5). The AF has the same trend of $\log(G/R)$ from which it derives, as shown in the right plot of Fig. 5. The AF can be used as a range error pattern, which allows the mean error to be corrected depending on the distance which affects long-term QPE.

6 Variability of the AF

Section 5 has introduced a range-dependent correction based on one year measurements. This global correction provides reasonable results for long-term precipitation amount estimates, as demonstrated in Sect. 7. To be applied at shorter time scales, AF variability, depending on event type, is investigated. As is done in Sect. 5, range error is characterized by examining the G/R ratio trend as a function of the range, obtained for each rain gauge location, using calibrated radar data collected during a single event. Initially, rainfall events collected by Polar 55C during the 2008–2009 period are split into convective and stratiform cases. The distinction is based
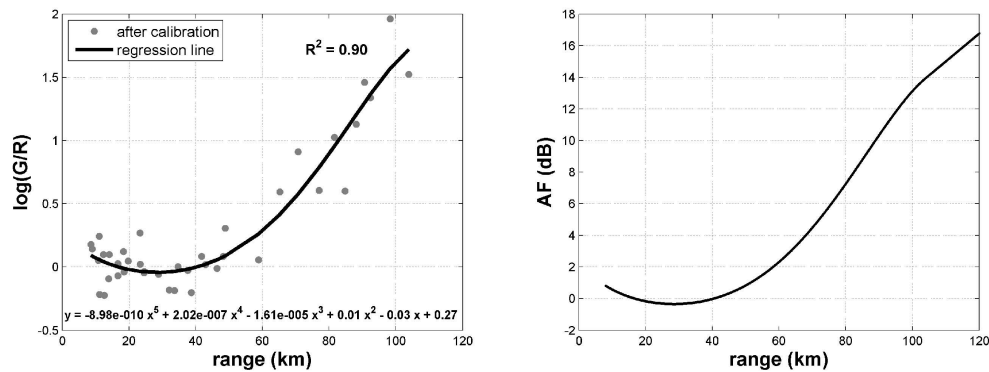
Fig. 5. Log(G/R) and adjustment factor (left and right panels, respectively) as a function of range resulting from observations at 1.5° elevations collected in 2008.

on a radar convective parameter (RCP), which takes into account the VPR distribution that characterizes each type of event (Steiner et al., 1995; Bechini et al., 2013). In each pixel to which one of the rain gauges of the network pertains, VPR is estimated through the use of a cycle of antenna elevation angles ranging from 1.5 to 5.5°. In this way, 40 VPR are acquired (i.e. as many as the rain gauges available) at time intervals of about 5 min, concerning a sampling volume between two isotherms corresponding to 0 and −15 °C. For each observed event, a RCP value is estimated as the root mean square error between the mean and the median of Z_h (in $mm^6\,m^{-3}$) values calculated at each sweep (Bechini et al., 2013). These differences, and thus the index, are smaller for stratiform cases than for convective cases. Events are thus divided into two classes (convective and stratiform) identified by the median of the index values set. In particular, an event is considered stratiform if its RCP is less than the 50th percentile and convective if its RCP is greater than the 50th percentile.

All events are chosen in such a way that rain is recorded by each rain gauge available, to avoid a lack of data preventing the plotting of the AF's curves with continuity. As a consequence, although several convective events are recognized (following the method described above) as having occurred during the summer season, we do not consider them because they are formed by sparse rain cells and the sampling by gauges is not sufficient. However, the methodology explained above also allows for the classification of certain events occurring during the cold season as convective. Investigating these events, we found that they are frequently formed by young cores of convective precipitation embedded into very wide stratiform rain areas, as is largely confirmed in the literature (Yuter and Houze, 1994; Houze, 1997; Vignal et al., 2000; Zhang et al., 2008; Zhang and Qi, 2010). Therefore, while a stratiform rain field is almost homogeneous, a convective one is quite variable in space. This explains the fact that the differences mentioned above are greater in cases of convective events than for stratiform ones. Moreover, dur-

ing each event at least a radiosonde that describes the vertical profile of the temperature is available.

Figures 6–11 describe some case studies concerning events classified as stratiform or convective by the methodology illustrated above. Solid and dashed lines shown in Figs. 6 and 9 are carried out after calibration, for each elevation angle, from the logarithm of the G/R ratio trend with range, by using a polynomial fit of the fifth order and a method of moving averages with a window of 15 km, respectively. Subsequently, values assumed by each curve are converted to dB. Moreover, curves have been drawn up to the limit of the rain field detectable by the radar in order to avoid the interpolation process possibly generating a non-meaningful overestimation of the corrective term.

Figures 8 and 11 show reflectivity measurements collected at vertical incidence by Polar 55C during a stratiform event and a convective one, respectively. In the convective case VPR refers to the stratiform part of precipitation, as we are interested in melting layer effects (see Sect. 6.2), namely bright band. In fact, inside convective cells the bright band signature is not defined because the intense updraft stops the formation of a melting layer (Steiner et al., 1995; Bordoy et al., 2010). Both figures show that the bright band peak is below the freezing level, which is shown taking into account the 162-m altitude of the radar antenna. The 0° isotherm heights are obtained by interpolating two consecutive temperature profiles carried out by the Pratica di Mare sounding station, located 27 km south of the radar site. Moreover, bright band thickness is a few hundred metres, as is largely explained in the literature (Mittermaier and Illinghworth, 2003; Baldini and Gorgucci, 2006; Zhang et al., 2008; Zhang and Qi, 2010; Bordoy et al., 2010; Krajewski et al., 2011). Above the freezing level, the reflectivity decreases with height due to the sampling of ice particles and beam overshooting (Seo et al., 2000). Below the bright band, reflectivity decreases until the DSD reaches a balance due to the ice melting, and the hydrometeors' volume decreases as the altitude decreases. Furthermore, vertical observations are considered as valid
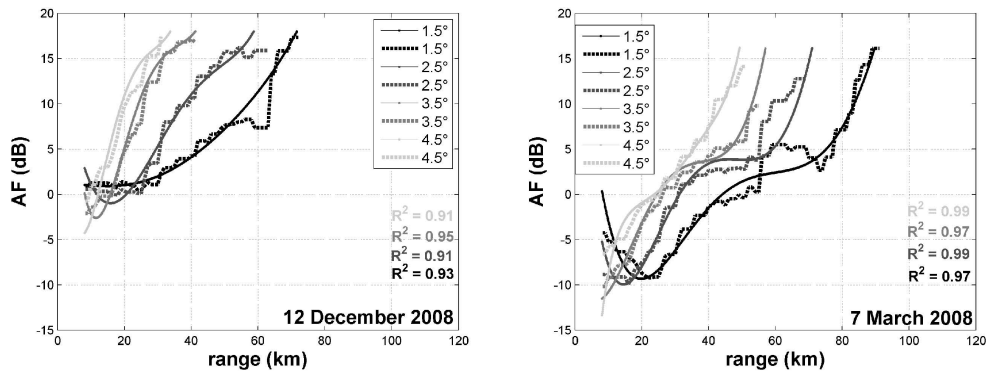
Fig. 6. AF trends with range carried out for the 12 December 2008 and the 7 March 2008 stratiform events, computed by using both a polynomial fit of the fifth order (solid lines) and a method of moving averages with a window of 15 km (dashed curves). Curves are obtained for different elevation angles ranging from 1.5 to 5.5°.

only from 800 m, due to the transient of polarization switch (Baldini and Gorgucci, 2006). For these reasons, following Zhang et al. (2008) and Krajewski et al. (2011), the VPR is considered independent from altitude. The reflectivity peak's altitude corresponds to the maximum in the VPR, while the top and the bottom bright band's borders are individuated by the minimums of the curvature of the Z_h profile below and above the peak's altitude (Drummond et al., 1996; Baldini and Gorgucci, 2006).

6.1 Stratiform events

During stratiform events, if the radar beam passes through the melting layer, radar overestimates rain in a range of distances which depends on the elevation angle. This range is relatively close to radar location, where the effects of attenuation and range degradation are negligible. Vice versa, at farther distances the probability that radar samples in a region above the precipitation or filled by ice particles increases, because of the radar beam propagation geometry. Furthermore, attenuation due to rain or to the presence of mixed phase in the melting layer reduces signal power. As a consequence radar tends to underestimates rainfall prior to correction. It follows that two different AF behaviours could be recognizable when stratiform events occur. In fact, AF curves in Fig. 6 consist of two parts: a concave portion at closer ranges due to the presence of the bright band (where the lowest values are found) and an almost-increasing linear one due to range errors. It must be noted that the greater the elevation angle (1) the lower the distance at which the radar beam intercepts the melting layer, (2) the shorter the path needed for the radar beam to pass through the melting layer, (3) the bigger the part sampled by the radar within the melting layer, and (4) the greater the slope of the second part of the curves, due to the greater effect of range degradation. As a consequence, as the elevation angle increases, the length of the concave part becomes shorter and the minimum value decreases and moves to the origin of the coordinate system, which corre-

sponds to radar site. Figures 6 and 9 also show the coefficient of determination, R^2, concerning the polynomial fit. For each elevation angle, the high values of R^2 mean that the best fitting lines are very suitable to represent the trend of $\log(G/R)$ (dB) as a function of range. There is also a substantial agreement between solid and dashed lines in both Figs. 6 and 9. Furthermore, the lightest grey curves in Fig. 6 do not show a concave part, meaning that during the events the bright band is intercepted at a distance less than that of the nearest rain gauge.

The event occurring on 12 December 2008 is a coolseason, wide-spread stratiform precipitation system lasting from midnight to 07:15 a.m. Figure 7 shows rain rate (mm h^{-1}) maps obtained by converting the reflectivity factor measured at the different sweeps composing a volume scan at 03:10 a.m. As shown by this figure, the vertical structure of precipitation is nearly uniform horizontally, except for the highest rain rate ring-shaped region indicating the bright band. By comparing the rainfall maps in Fig. 7 with the corresponding curves in Fig. 6, it can be seen that the locations of the bright band with respect to the radar site closely correspond to the ranges where AF curves present their concavity upwards (considering that Fig. 7 refers only to a PPI, whereas Fig. 6 to the whole event). Figure 8 shows the 0 °C isothermal, located at a height of 1650 m a.s.l., and the VPR, both referring to 03:10 a.m. Bright band is between 0.75 km and 1.3 km above the antenna. When the antenna angle passes from 1.5 to 5.5°, the distances in which the radar beam intercepts the melting layer calculated from the bright band bounds altitudes ranges from about 27 to 44 km, 17 to 28 km, 12 to 20 km, and 9 to 16 km, respectively, corresponding to the thickness of the reflectivity rings in Fig. 7.

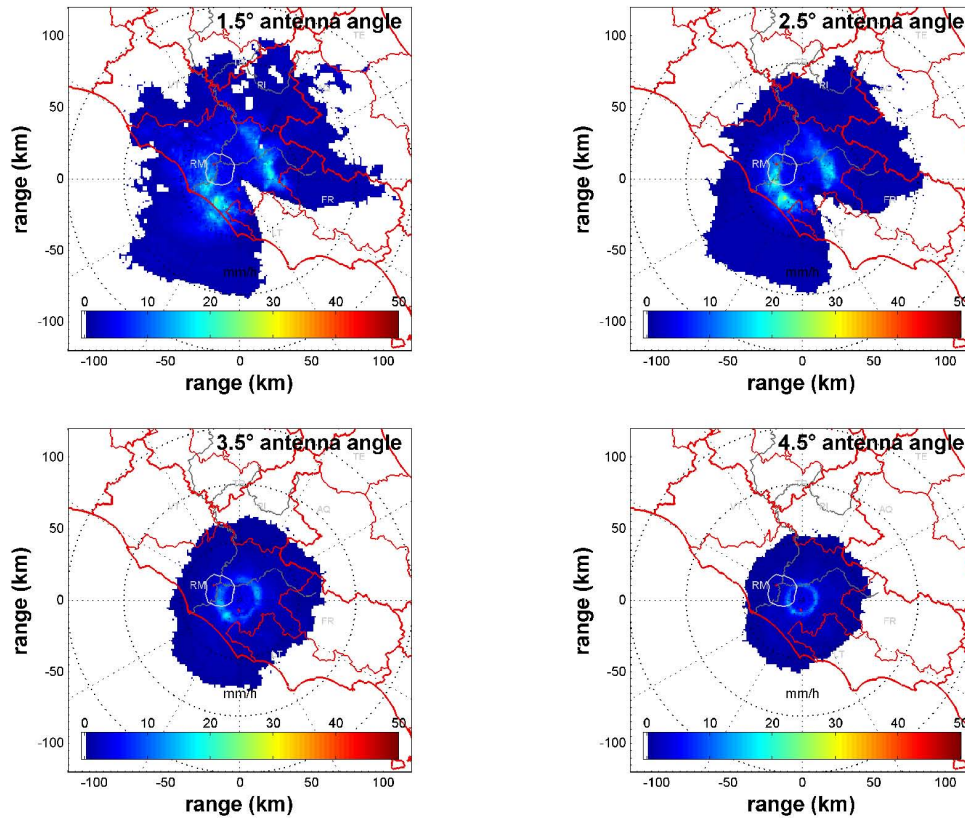The same considerations are valid for the other stratiform event (not shown).

Fig. 7. Rain rate (mm h^{-1}) maps obtained during a volume scanning at 03:10 a.m. during the stratiform event of 12 December 2008. Note that sector delimited by azimuth 130 and 150° is screened by nearby hills.
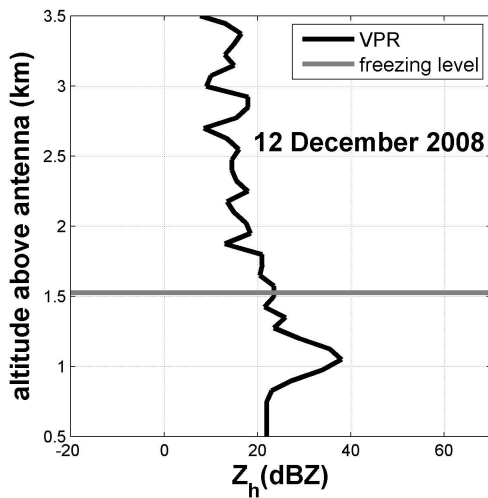

Fig. 8. Reflectivity as a function of altitude (km) and 0°C isothermal height at 03:10 a.m., both relative to the stratiform event of 12 December 2008.

6.2 Convective events

Convective events here considered occur in the cold season as young cores of convective rain embedded inside a wide stratiform precipitation region, as described above. Depending on the vertical profile of temperature, the stratiform part of precipitation could determine the occurrence of a distinctive melting layer signature, as it happens in the cases in point. For these reasons, curves in Fig. 9 obtained for cold-season convective events have trends qualitatively similar to those in Fig. 6, which are related to stratiform events. However, by comparing plots of Figs. 6 and 9, it can be noted that generally, the length of the AF curves is greater for convective cases than for stratiform ones. This is due to the fact that radar can more easily sample above the stratiform precipitation because cloud tops are lower during stratiform events than the cumulonimbus cloud tops of convective events (Yuter and Houze, 1994; Steiner et al., 1995; Houze, 1997). Furthermore, the coordinates of the minimum point of the concave part does not have a clear dependence on the elevation. Unlike the stratiform cases, as the elevation increases the ordinate can also increases. Instead, the abscissa becomes progressively smaller, as already shown for stratiform cases, even if in some convective cases it slightly decreases, as in
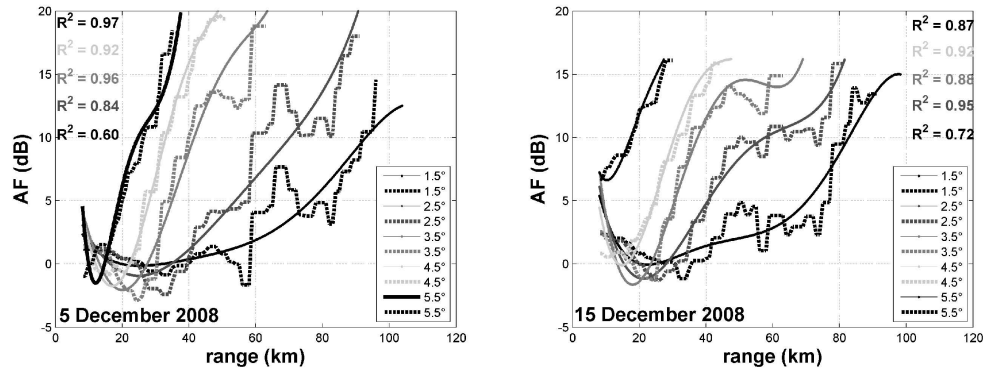
Fig. 9. AF trends with range computed for the 5 December 2008 and the 15 December 2008 cold-season convective events by using both a polynomial fit of the fifth order (solid lines) and a method of moving averages with a window of 15 km (dashed curves). Curves are obtained for different elevation angles ranging from 1.5 to 5.5°.
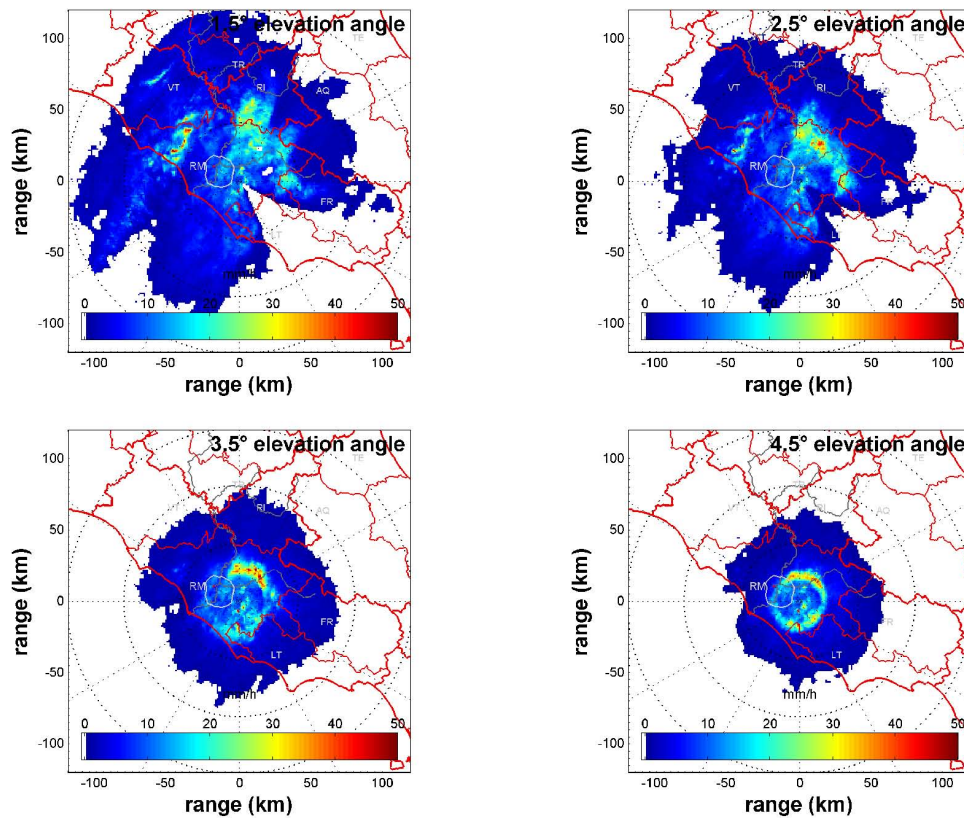

Fig. 10. Rain rate (mm h^{-1}) maps obtained from a volume scanning at 15:40 p.m. during the convective event of 5 December 2008.

the event of 15 December 2008. This is probably due to the fact that the stratiform part of the rainfall field is discontinuous and non-uniform in space.

The convective event occurring on 5 December 2008 has a length of 8 h, from 10:00 a.m. to 18:00 p.m. Precipitation is formed by a convective part situated both to the north-east and to the north-west of the Rome urban area, and convective cells are embedded in a larger stratiform precipitation region.

By comparing each curve in Fig. 9 with the relative rainfall map (Fig. 10), it can be seen that the positions of the bright band with respect to the radar site roughly correspond to the ranges where AF curves present their concavity upwards. The freezing level is located at a height of 2055 m a.s.l. at 15:40 p.m., which is the time corresponding to the PPIs in Fig. 10. The VPR collected at the same time by Polar 55C at vertical antenna is represented in Fig. 11, together with
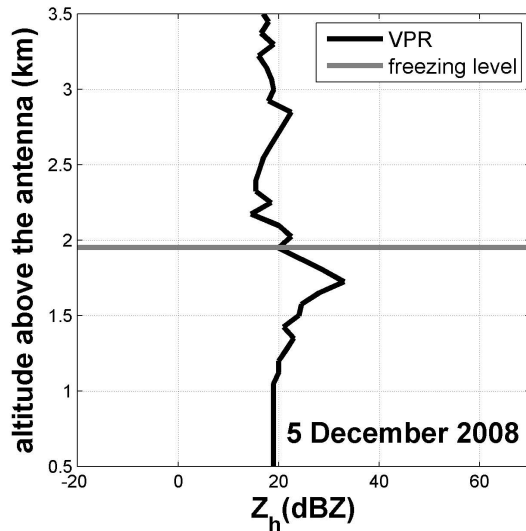
Fig. 11. Reflectivity trend with altitude (km) and 0°C isothermal height at 15:40 p.m., both relative to the stratiform part of the convective event of 5 December 2008.

the 0 °C isothermal height. The figure shows that the freezing level is between 1.4 km and 1.9 km above the antenna. The distances where the radar beam intercepts the melting layer are calculated from the top and the bottom altitudes of the bright band. When the elevation angle moves from 1.5 to 5.5°, they range from about 48 to 63 km, 30 to 41 km, 22 to 30 km, and 18 to 24 km, respectively, corresponding to the reflectivity rings thickness shown in Fig. 10.

The same considerations are valid for the other convective event (not shown).

6.3 A global AF

The AF shows a trend with range that is qualitatively similar for events of the same category. However, at a given range there are significant quantitative differences between the values it assumes for events of the same type. So, there is not an univocal range error pattern at the scale of event. The AF depends not only on the event type, being also a function of the spatial extension of the event, of the radar elevation angle, of the vertical profile of temperature, and of the presence and characteristics of bright band. All these characteristics vary with time within the same event and would require correction at very short time scales, if not in real time. Since our goal is long-term rainfall amount quantification, the AF has been evaluated as a function of corresponding radar and rain gauge annual rainfall amounts calculated at each rain gauge location, as shown in Sect. 5. Consequently, the verification of the effectiveness of the proposed methodology is performed by calculating the annual rainfall amounts at each rain gauge location. This choice is based on the observation that the AF tends to become gradually more stable with increasing accumulation time, at equal elevation, as can be observed from
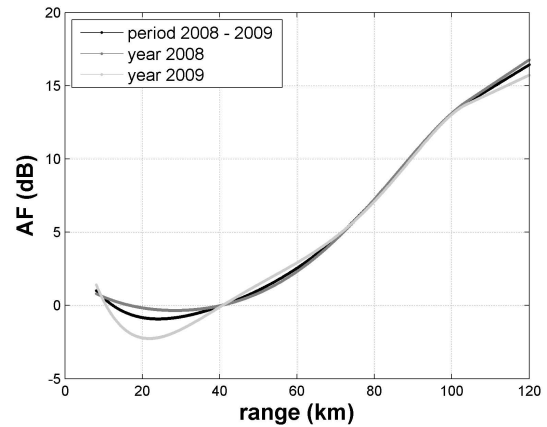

Fig. 12. AF trends with range evaluated for longer accumulation times (black, dark grey, and light grey refer to the period 2008–2009, the year 2008, and the year 2009, respectively) and the antenna elevation angle of 1.5°.

Fig. 12, which shows a substantial agreement between AF curves estimated for longer accumulation times (one year or two years).

As a consequence, the model proposed in Sect. 5 is suitable for applications that require long-term precipitation estimates (mm), such as the quantitative estimation of precipitation necessary to evaluate the water budget of a basin.

7 Verification of the adjustment procedure

Radar data are corrected by means of the isotropic range dependent bias, AF, estimated by using data collected in 2008 (Sect. 5). The correspondence between pairs of rainfall processes observed by radar and by each rain gauge at the rain gauge site is investigated through the analysis of trend with range from Polar 55C of the (1) FSE index; (2) slope of the scatter plots' regression lines; and (3) G/R ratio between rain gauges' and radar rainfall amounts, defined as in Eq. (6). Each index value can be defined by choosing a pair of rainfall processes observed at the same time by the radar and by a rain gauge at the rain gauge location. In particular, FSE values are calculated by computing the differences between pairs of rainfall time series selected as previously described, which are compared also in a scatter plot. The slope of the regression line is then calculated for each scatter plot. Since a scatter plot concerns the comparison between data from radar and only one rain gauge, and as each rain gauge is located at a different distance from radar, it has been possible to relate the regression lines' slope to the range. At each rain gauge site, the G/R ratio between a rain gauge rainfall amount G and the corresponding radar rainfall amount R is computed and plotted against the distance from radar of each rain gauge.

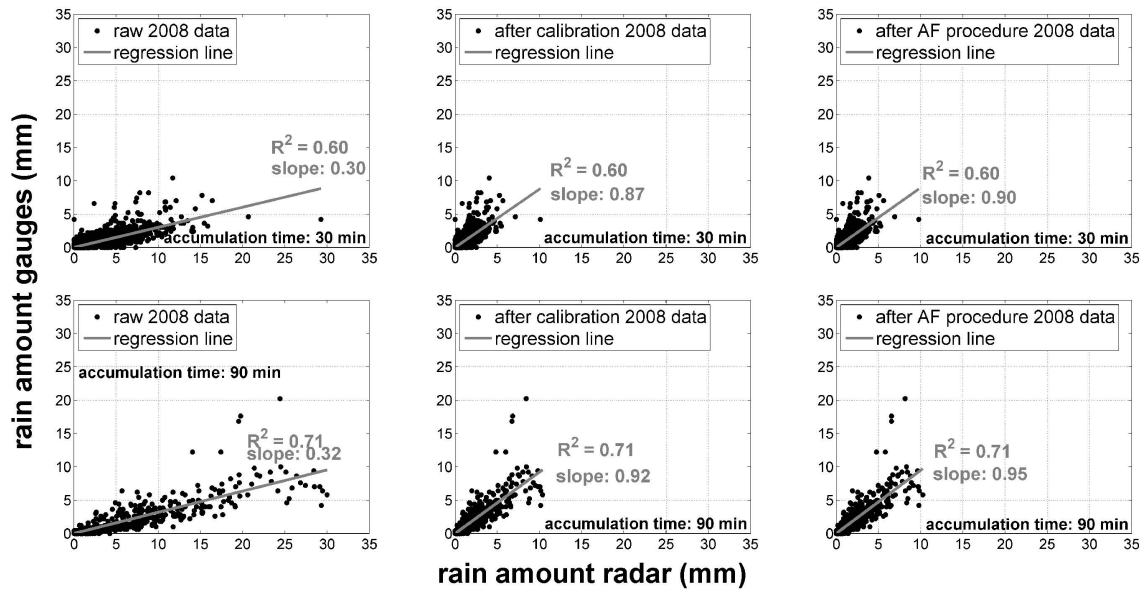The FSE is used here as a measure of the differences between the values predicted by a model (namely radar data)

Fig. 13. Scatter plots of rainfall time series' pairs, obtained during 2008 by Polar 55C and by each rain gauge located from 25 to 40 km away from Polar 55C. These refer to a time aggregation of 30 and 90 min (upper panels and lower panels, respectively) for the initial data sets (left panels), after calibration (middle panels) and after the adjustment procedure (right panels).

and the values actually observed from a rain gauge, or to quantify the radar error. It is defined as follows:

$$\text{FSE} = \frac{\sqrt{\sum\limits_{i=1}^{N} (x_r - x_g)^2 \big/ N}}{\sum\limits_{i=1}^{N} x_g \big/ N}, \tag{9}$$

where x_r and x_g are the radar and the rain gauge data, respectively, while N is the number of the observed values.

To verify the effectiveness of the methodology, the spatial dependence of rainfall radar field is characterized by analysis of behaviour (in relation to the slant range) of the above-mentioned variables, which are calculated both for the 2008 data sets and for the 2009 data sets. Trends against the range obtained both before and after the adjustment procedure are compared to show the improvement of radar estimates. Each comparison is performed by considering a fixed accumulation time, ranging from 30 to 90 min. Moreover, we analyse the scatter plots for two ranges of distances where different radar errors prevail, namely 0–40 km and 40–120 km.

Radar data sets are used with different processing levels, namely without any correction, after radar calibration and after the adjustment procedure.

Scatter plots in Figs. 13 and 14 concern rain gauges located within the range of distances from 25 to 40 km away from Polar 55C, where the radar beam intercepts the melting layer most frequently during the cold season at the elevation angle of 1.5°. The rainfall time series of Fig. 13 and Fig. 14 have been observed during 2008 and during 2009, respec-

tively. These figures concern accumulation times of both 30 min (upper panels) and 90 min (lower panels). The plots on the left represent the measured (raw) radar data. The plots in the middle and the plots on the right are obtained after radar calibration and after adding the AF to the reflectivity, respectively. Since the effects of sampling uncertainties and attenuation are negligible close to the radar, it must be noted that prior to calibration Polar 55C overestimates rainfall with respect to rain gauges, due to radar miscalibration and the presence of melting layer. Then, calibration strongly reduces radar overestimation. In fact, by comparing left panels and graphs in the middle both in Fig. 13 and in Fig. 14, the regression line's slope strongly increases after calibration. After applying the AF to reflectivity maps, rainfall radar estimates slightly improve again, because also the effect of melting layer is corrected. In fact, a further increase of the slope occurs when the AF is added to reflectivity. In Fig. 13, when accumulation time passes from 30 to 90 min, the slope increases from 0.30 to 0.90 (upper panels) and from 0.32 to 0.95 (lower panels). At the same time, in Fig. 14 the regression line's slope change from 0.28 to 0.83 (upper panels) and from 0.30 to 0.91 (lower panels).

At longer distances and prior to calibration, overestimation due to miscalibration effects is compensated for by the effects of sampling errors and attenuation (which would lead to rainfall underestimation). Moreover, melting layer effects do not exist, but likely ice (but not rain) is sampled. Therefore, before calibration, when the radar samples beyond a distance of 40 km, it overestimates rain less than in the previous case. This may be observed by comparing left plots
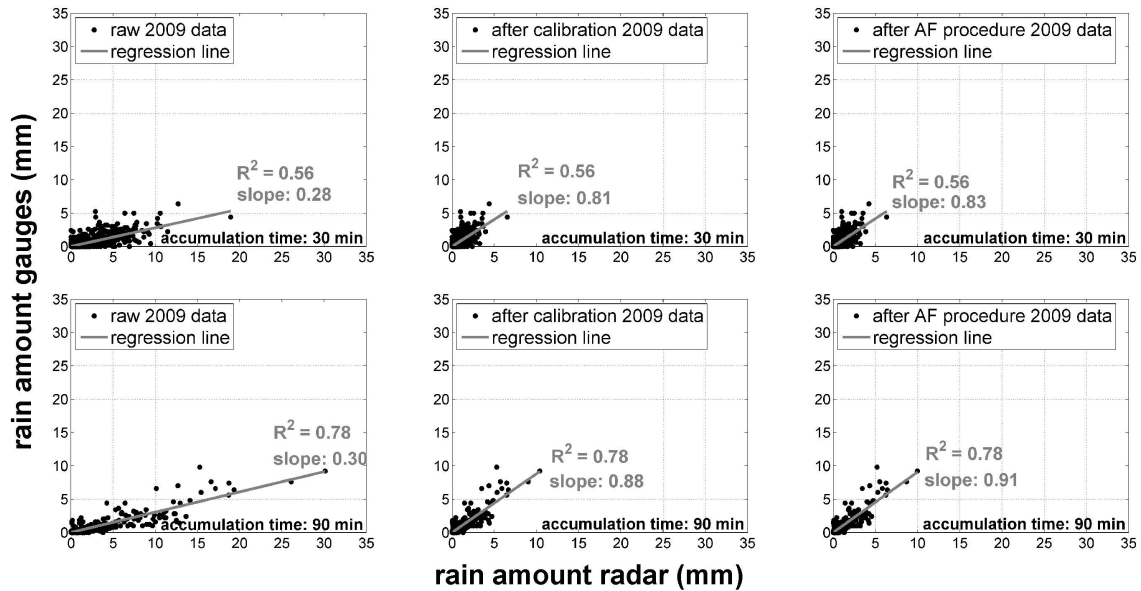
Fig. 14. Scatter plots of rainfall time series' pairs, obtained during 2009 by Polar 55C and by each rain gauge located from 25 to 40 km away from Polar 55C. These refer to a time aggregation of 30 and 90 min (upper panels and lower panels, respectively) for the initial data sets (left panels), after calibration (middle panels) and after the adjustment procedure (right panels).
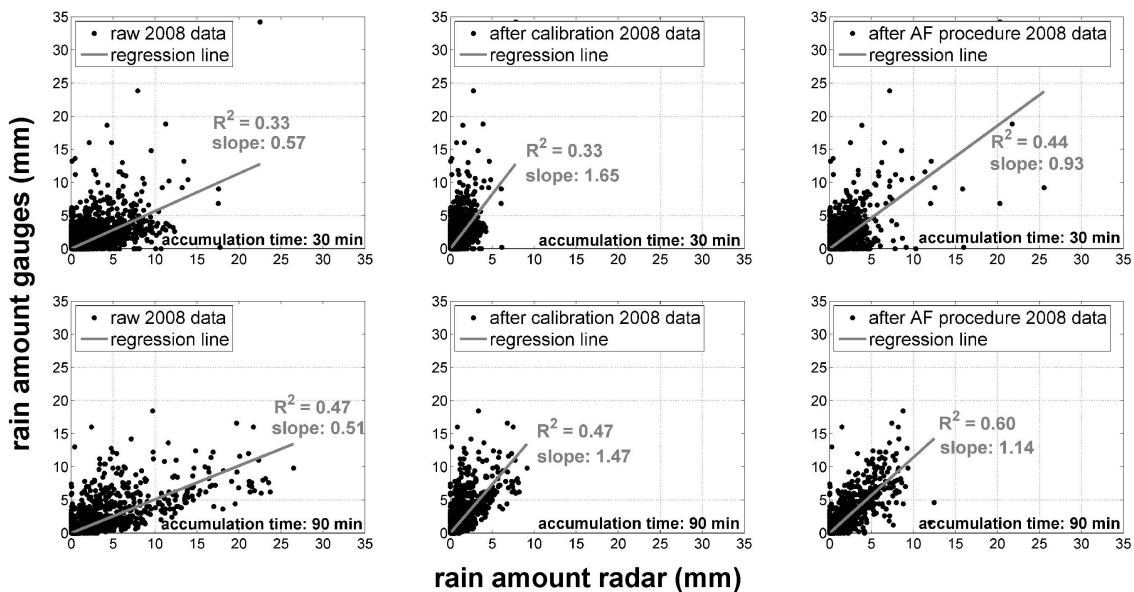

Fig. 15. Scatter plots of rainfall time series' pairs, obtained during 2008 by Polar 55C and by each rain gauge located beyond a distance of 40 km from radar. These refer to a time aggregation of 30 and 90 min (upper panels and lower panels, respectively) for the initial data sets (left panels), after calibration (middle panels) and after the adjustment procedure (right panels).

in Figs. 13 and 15, or left plots in Figs. 14 and 16. Rainfall time series in Figs. 15 and 16 refer to measurements collected beyond a distance of 40 km from Polar 55C in 2008 and in 2009, respectively. In particular, left, middle and right panels refer to different processing levels, namely raw reflectivity, calibrated reflectivity, and after applying the adjustment procedure, respectively. Upper and lower panels refer to 30-

and 90-min accumulation times, respectively. Once calibration is performed, at farther distances the effects of range errors are no longer compensated for, and radar underestimates rainfall. In particular, by comparing left and middle panels in Fig. 15, it results that the slope of the regression lines increases by about 1 or 1.1, depending on the accumulation time. Instead, for 2009 data, it increases by about 1 or
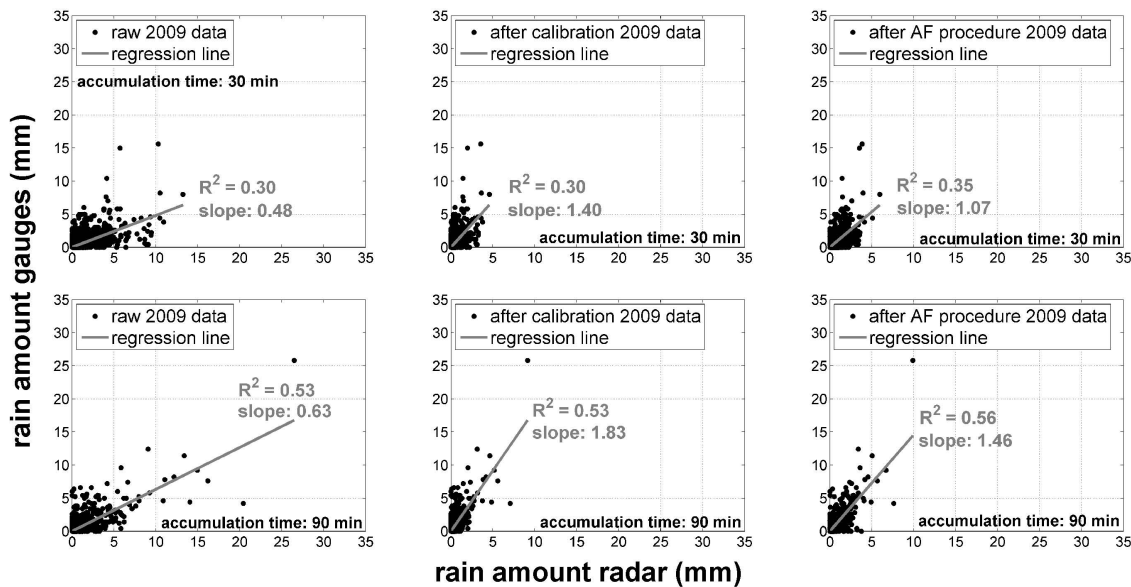
Fig. 16. Scatter plots of rainfall time series' pairs, obtained during 2009 by Polar 55C and by each rain gauge located beyond a distance of 40 km from radar. These refer to a time aggregation of 30 and 90 min (upper panels and lower panels, respectively) for the initial data sets (left panels), after calibration (middle panels) and after the adjustment procedure (right panels).

1.2, referring to 30-min and 90-min accumulation time, respectively (compare corresponding plots in Fig. 16). Then, by comparing the slopes of the regression lines in middle and right panels in Figs. 15 and 16, it can be seen that, after adding the AF to reflectivity, rainfall radar estimates always improve due to the range errors correction. Therefore, in Fig. 15 slope values pass from 1.65 to 0.93 and from 1.47 to 1.14 for 30-min and 90-min accumulation times, respectively. Correspondingly, in Fig. 16, they pass from 1.40 to 1.07 and from 1.83 to 1.46.

In addition, by observing Figs. 15 and 16, it can be noted that coefficient of determination R^2 increases when the AF is added to reflectivity. This is due to the fact that the AF increases as the distance from radar increases (see Fig. 5). So, radar estimates performed close to the edge of the scanning circle (where the underestimation is greatest) increase more than other values after correction. Thus, at the end of the adjustment procedure, dots are less scattered, meaning that correlation increases, and, therefore, R^2 increases (Kottegoda and Rosso, 2008). Vice versa, close to Polar 55C, as shown by Figs. 13 and 14, R^2 does not increases when the AF is added to reflectivity, because the AF is not so variable within the range of distances considered, as shown in Fig. 5. Finally, the correlation between radar and rain gauges' rainfall time series always increases as the accumulation time increases.

Figure 17 shows trends of the FSE, slope of the scatter plots' regression lines and the G/R ratio as a function of the range, estimated for radar and rain gauges' data sets collected during 2008 (upper panels) and 2009 (lower panels). Each plot shows three curves, each of them relative to a different

radar data set, obtained before any correction, after radar calibration and after the adjustment procedure (blue, green and red dots, respectively). Notably, the slope of the scatter plots' regression lines always has the same trend with range as with the G/R ratio.

Due to the radar rainfall overestimation, the FSE index and G/R ratio (or slope of the scatter plots' regression lines) have the greatest and the lowest values, respectively, (blue dots) at closer ranges. But, sampling errors and attenuation effects become more and more important as the distance increases until the radar miscalibration effect is balanced. Therefore, close to the edge of the scanned area Polar 55C can underestimate rainfall. In fact, the FSE reaches the maximum value for distances where more frequently the radar beam has intercepted the melting layer during the year. Similarly, the corresponding G/R and slope values reach a minimum value for the same distances. Then, the FSE begins to decrease up to a value of about 1, whereas the G/R ratio and slope begin to increase up to a value of 1 or more. For distances that range from about 70 to 90 km, the slope and G/R ratio are close to 1 because the radar miscalibration effect is balanced by the effects of path attenuation and radar sampling geometry. Beyond these distances the slope and G/R ratio slightly increase, reaching values ranging from 1 to 2 (in most cases) because range errors increase with distance exceeding bias. For this reason, beyond 70 km from radar the FSE trend is not so clear (as shown by blue dots in left panels in Fig. 17).

Moreover, through calibration the FSE decreases where effects of bias due to miscalibration prevail over range errors, while it increases where range errors exceed bias
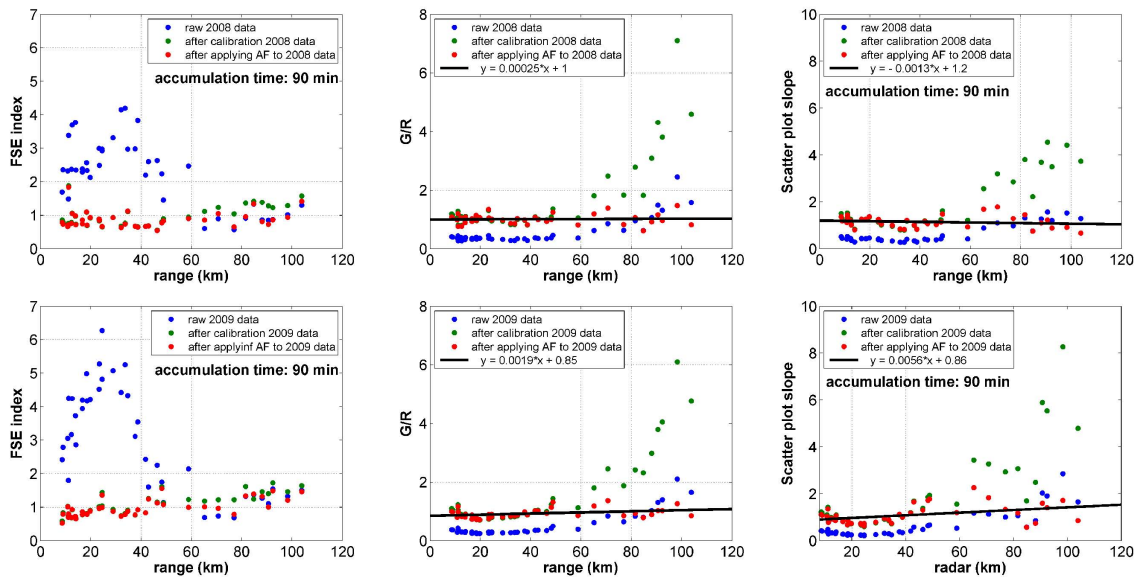
Fig. 17. FSE index, G/R ratio and slope of the scatter plots' regression lines' trends with distance (left, middle and right panels, respectively) of rainfall time series pairs obtained during 2008 (upper panels) and 2009 (lower panels) by Polar 55C and by each rain gauge, for the initial data sets (dots in blue), after calibration (dots in green) and after adding the AF (dots in red). Black lines are best fitting lines referring to red dots. Accumulation time is 90 min.

(comparison between blue and green dots in Fig. 17). At a fixed distance, the G/R ratio and slope always increase after performing calibration. As a result, they are about equal to 1 close to the radar, where the effects of sampling errors and attenuation are negligible. However, they take values lower than 1 within the area more subject to the bright band occurrence. But, beyond the range which corresponds to the presence of the melting layer, their values begin to increase up to a value of about 5 or more, due to range errors. At the end of the adjustment procedure, they are close to 1 all along the path, due to the improvement of radar estimates. In fact, when the AF is added to reflectivity, the G/R ratio and slope decrease far from radar due to the correction of range errors, and they tend to increase, albeit slightly, where the bright band is corrected. Correspondingly, the FSE index has the lowest values, as shown by red dots in Fig. 17, which demonstrate the increased agreement between radar and rain gauge rainfall fields. In particular, close to the radar, FSE values become close to 1 or less after the adjustment procedure, whereas they can be up to 4 or more before calibration where the radar beam most probably intercepts the melting layer. At far distances, FSE values range from 1 to 2, after calibration, but they decrease after the adjustment procedure. Curves in Fig. 17 are obtained by considering an accumulation time of 90 min. The improvement of radar estimates is confirmed also by the slopes of the best fitting lines (referring to red dots) represented in black, which are very close to 1.

Figure 18 shows the FSE (top) and the slope of the scatter plots' regression lines' (bottom) trends against range of rainfall time series pairs obtained during 2009 by Polar 55C and

each rain gauge, for the initial data set, after calibration and after the adjustment procedure (left, middle and right panels, respectively). The dots' colours refer to different accumulation times (30, 60 and 90 min). Figure 18 shows that both the slope of the scatter plots' regression lines and the FSE index maintain the same trend against range for each accumulation time. So, the improvement of radar estimates is obtained for all the accumulation times considered in this work (as already illustrated in Figs. 13, 14, 13, and 16).

As mentioned above, rainfall radar estimates slightly improve when the effect of the melting layer is corrected by adding the AF to the reflectivity. To highlight this improvement we compute the differences between the values that the variables represented in Fig. 17 take before and after the AF is added to reflectivity, within the range of distances where the bright band signature is recognizable. Figure 19 shows these differences concerning the 2009 data and an accumulation time of 30 min. The subscripts C and AF refer to two different processing levels, namely after calibration and at the end of the adjustment procedure. It can be seen that, after the addition of the AF to reflectivity, the G/R ratio and scatter plots' regression lines' slope increase, whereas the FSE index decreases because of the correction of radar overestimation due to the sampling within the melting layer.
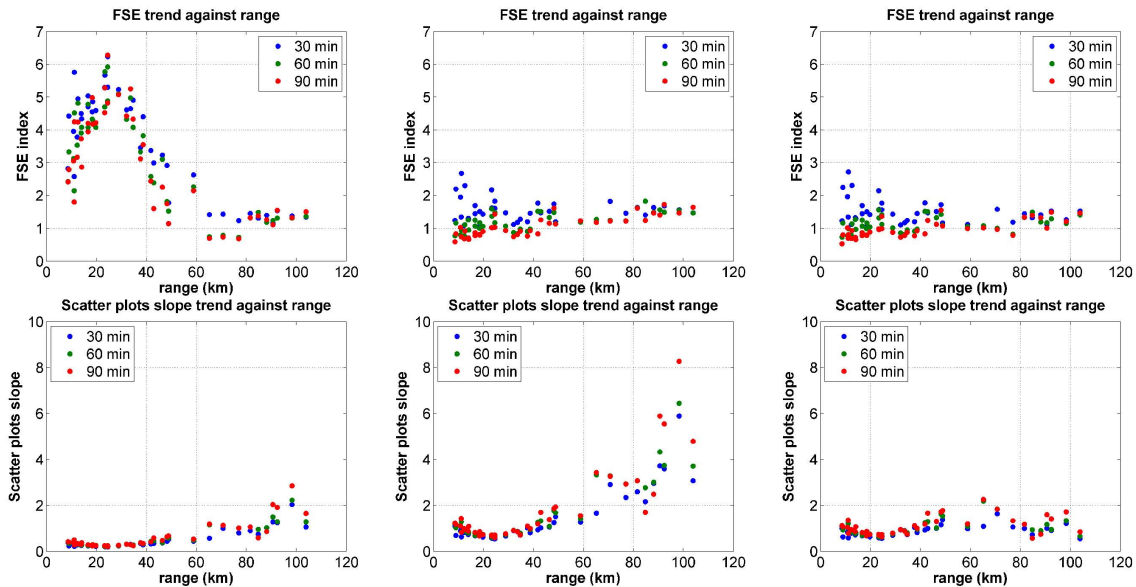
Fig. 18. FSE trend and slope of the scatter plots' regression lines' trend with range (plots on the top and on the bottom respectively) of rainfall time series pairs obtained during 2009 by Polar 55C and by each rain gauge for the initial data sets, after calibration, and after the adjustment procedure (left panels, middle panels and right panels, respectively). Dots in blue, in green and in red correspond to an accumulation time of 30, 60 and 90 min, respectively.
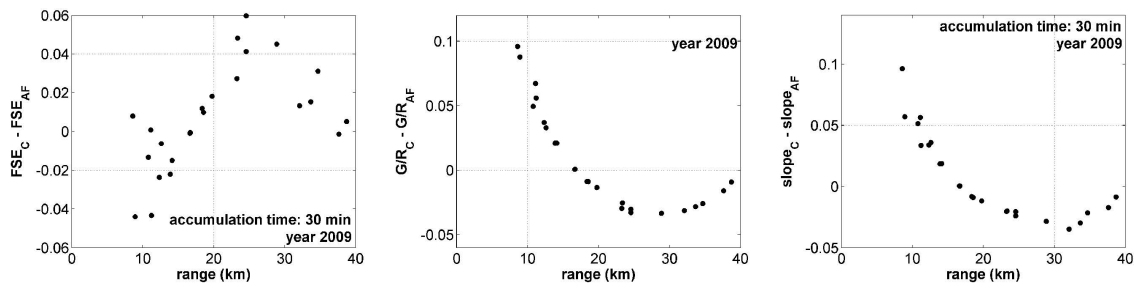

Fig. 19. Differences between FSE, G/R, and slope values before and after the AF correction, within the range of distances 0–40 km. Figure refers to the year 2009. Subscripts C and AF refer to two different processing levels, namely after calibration and at the end of the adjustment procedure.

8 Conclusions

There are several error sources that influence the accuracy of radar rainfall estimates: error is expected, on average, to increase as the distance from radar increases. This paper has characterized this overall error as a function of the slant range, to improve radar estimates in the absence of orographic effects. This technique, intended to quantify radar error, considers rain gauges' direct rainfall measurements as "ground truth". The proposed methodology has been developed and evaluated using radar data sets of measurements collected at the elevation of 1.5° degrees by the Polar 55C radar located in Rome and data from the rain gauge network within the radar coverage. Areas where residual influence of ground clutter or beam blocking can affect radar estimates

are excluded, in order to address the error sources that can lead to characterization as a function of the range.

To reach this objective, first radar is calibrated using six rain gauges, whose distances from Polar 55C are from 15 to 20 km, with good visibility from the radar.

The G/R ratio between the rain gauges' rainfall amounts and the respective radar rainfall amounts is then calculated as a function of range. Within the range of about 50 km, the G/R trend is influenced by the presence of the bright band, which causes an overestimation of radar rain. But, beyond this range, an approximately logarithmic trend against distance of the G/R ratio occurs. A best fitting line of the logarithm of G/R is used to define an adjustment factor depending on the range, which takes the overall radar error into account. The AF curve is composed of a concave portion

relative to closer ranges and an almost monotonically increasing one for farther ranges.

The AF variability is investigated at the scale of event, both for convective and stratiform cases also as a function of elevation angle. We found similarities for both categories. The minimum point of each curve tends to move towards the origin of the axes, and the concave portion becomes less wide as the elevation angle increases. In addition, only for the stratiform cases, the minimum value decreases as the antenna elevation increases. The latter fact does not occur for convective cases because of the discontinuity of the bright band. Therefore, on one hand the model is extremely variable, depending on the particular characteristics of the considered event. On the other hand, it tends to stabilize itself for time aggregations of the order of one year or greater. As a consequence, radar data are corrected by means of the isotropic range dependent bias, AF, estimated by using yearly data.

Radar calibration is performed using the 2008 radar data set without any correction. Then, radar data are corrected by means of the AF estimated from the 2008 calibrated radar data set. The verification of the adjustment procedure is carried out by considering both 2008 and 2009 radar data sets.

The performance of the AF is evaluated from the behaviours as a function of range of the FSE index, slope of the scatter plots' regression lines and G/R ratio of rainfall time series pairs, obtained during 2008 or 2009 by Polar 55C and by each rain gauge. The slope of the scatter plots' regression lines and the G/R ratio have the same trend against distance for each accumulation time.

Before calibration, the FSE reaches the maximum value (even greater than 4) for distances where more frequently the radar beam intercepts melting layer. Similarly, the corresponding G/R and slope values reach a minimum value for the same distances. Then, the FSE begins to decrease up to a value of about 1, whereas the G/R ratio and slope begin to increase up to a value of 1 or more. After the adjustment procedure, all along the path the G/R ratio and the slope of the scatter plots' regression lines are scattered about 1, and the FSE index gives the lowest values for each accumulation time, due to the reduction of the discrepancies between radar and rain gauge rainfall fields. The simple approach proposed in this paper can be used to extend the use of radar rainfall for applications that require long-term quantitative precipitation estimates.

References

Baldini, L. and Gorgucci, E.: Identification of the Melting Layer through Dual-Polarization Radar Measurements at Vertical Incidence, J. Atmos. Ocean. Tech., 23, 829–839, 2006.

Barber, P. and Yeh, C.: Scattering of electromagnetic waves by arbitrarily shaped dielectric bodies, Appl. Opt., 14, 2864–2872, 1975.

Bechini, R., Baldini, L., and Chandrasekar, V.: Polarimetric radar observations in the ice region of precipitating clouds at C-band and X-band radar frequencies, J. Appl. Meteorol. Clim., doi:10.1175/JAMC-D-12-055.1, in press, 2013.

Berenguer, M. and Zawadzki, I.: A study of the error covariance matrix of radar rainfall estimates in stratiform rain, Weather Forecast., 23, 1085–1101, 2008.

Berenguer, M. and Zawadzki, I.: A study of the error covariance matrix of radar rainfall estimates in stratiform rain. Part II: scale dependence, Weather Forecast., 24, 800–811, 2009.

Bordoy, R., Bech, J., Rigo, T., and Pineda, N.: Analysis of a method for radar rainfall estimation considering the freezing level height, Journal of Mediterranean Meteorology & Climatology, 7, 25–39, 2010.

Borga, M. and Tonelli, F.: Adjustment of range-dependent bias in radar rainfall estimates, Phys. Chem. Earth, 25, 909–914, 2000.

Brandes, E. A., Vivekanandan, J., and Wlison, J. W.: A comparison of radar reflectivity estimates of rainfall from collocated radars, J. Atmos. Ocean. Tech., 16, 1264–1272, 1999.

Bringi, V. N. and Chandrasekar, V.: Polarimetric Doppler weather radar: principles and applications, Cambridge University Press, New York, USA, 2001.

Clothier, A. and Pegram, G.: Space-time modelling of rainfall using the string of beads model: integration of radar and raingauge data, Water Research Commission, Durban, South Africa, WRC Rep. No. 1010/1/02, 166 pp., 2002.

Delrieu, G., Braud, I., Berne, A., Borga, M., Buodevillain, B., Fabri, F., Freer, J., Gaume, E., Nakakita, E., Seed, A., Tabary, P., and Uijlenhoet, R.: Weather radar and hydrology, Adv. Water Resour., 32, 969–974, 2009.

Drummond, F. J., Rogers, R., Cohn, S. A., Ecklund, W. L., Carter, D. A., and Wilson, J. S.: A new look at the melting layer, J. Atmos. Sci., 53, 759–769, 1996.

Gabella, M. and Amitai, E.: Radar rainfall estimates in an Alpine environment using different gage-adjustment techniques, Phys. Chem. Earth, 25, 927–931, 2000.

Gabella, M., Joss, J., Perona, G., and Galli, G.: Accuracy of rainfall estimates by two radars in the same Alpine environment using gage adjustment, J. Geophys. Res., 106, 5139–5150, 2001.

Giangrande, S. E. and Ryzhkov, A. V.: The quality of rainfall estimation with the polarimetric WSR-88D radar as a function of range, in: Proceedings of the 31st Int. Conf. on Radar Meteorology, Seattle, WA, Amer. Meteor. Soc., 357–360, 2003.

Giangrande, S. E. and Ryzhkov, A. V.: Calibration of dual-polarization radar in the presence of partial beam blockage, J. Atmos. Ocean. Tech., 22, 1156–1166, 2005.

Giangrande, S. E. and Ryzhkov, A. V.: Estimation of rainfall based on the results of polarimetric echo classification, J. Appl. Meteorol. Clim., 47, 2445–2462, 2008.

Gjertsen, U., Salek, M., and Michelson, D. B.: Gauge adjustment of radar-based precipitation estimates in Europe, in: Proceedings of the 3rd European Conference on Radar in Meteorology and

Hydrology ERAD, Visby, Sweden, 6–10 September 2004, 7–11, 2004.

Gorgucci, E. and Baldini, L.: An examination of the validity of the mean raindrop-shape model for dual-polarization radar rainfall retrievals, IEEE T. Geosci. Remote, 47, 2752–2761, 2009.

Gorgucci, E., Scarchilli, G., and Chandrasekar, V.: Radar and surface measurements of rainfall during CaPE, J. Appl. Meteorol., 34, 1570–1577, 1995.

Gorgucci, E., Baldini, L., and Volpi, A.: Polar 55C: an upgraded instrument for polarimetric radar research, in: Proceedings of the 2nd European Conference on Radar in Meteorology and Hydrology ERAD, Delft, The Netherlands, 18–23 November 2002, 394–399, 2002.

Ha, E. and Yoo, C.: Use of mixed bivariate distributions for deriving inter-station correlation coefficients of rainfall, Hydrol. Process., 21, 3078–3086, 2007.

Habib, E., Krajewski, W. F., and Ciach, G. J.: Estimation of rainfall interstation correlation, J. Hydrometeorol., 2, 621–629, 2001.

Houze J. R. A.: Stratiform precipitation in regions of convection: a meteorological paradox?, B. Am. Meteorol. Soc., 78, 2179–2196, 1997.

Junyent, F. and Chandrasekar, V.: Theory and characterization of weather radar networks, J. Atmos. Ocean. Tech., 26, 474–491, 2009.

Kendall, M. G.: Rank and product-moment correlation, Biometrika, 36, 177, 1949.

Kendall, M. G. and Stuart, A.: The advanced theory of statistics, vol. 2 Inference and relationship, Griffin, London, UK, 1973.

Koistinen, J. and Puhakka, T.: Can we calibrate radar with rain-gauges, Geophysica, 22, 119–129, 1986.

Kottegoda, N. T. and Rosso, R.: Applied statistics for civil and environmental engineers, Blackwell Publishing, Oxford, UK, 2008.

Krajewski, W. F., Vignal, B., Seo, B. C., and Villarini, G.: Statistical model of the range-dependent error in radar-rainfall estimates due to the vertical profile of reflectivity, J. Hydrol., 402, 306–316, 2011.

Lombardo, F., Napolitano, F., and Russo, F.: On the use of radar reflectivity for estimation of the areal reduction factor, Nat. Hazards Earth Syst. Sci., 6, 377–386, doi:10.5194/nhess-6-377-2006, 2006a.

Lombardo, F., Napolitano, F., Russo, F., Scialanga, G., Baldini, L., and Gorgucci, E.: Rainfall estimation and ground clutter rejection with dual polarization weather radar, Adv. Geosci., 7, 127–130, doi:10.5194/adgeo-7-127-2006, 2006b.

Maheepala, U. K., Takyi, A. K., and Perera, B. J. C.: Hydrological data monitoring for urban stormwater drainage systems, J. Hydrol., 245, 32–47, 2001.

Michelson, D. B. and Koistinen, J.: Gauge-radar network adjustment for the Baltic sea experiment, Phys. Chem. Earth (B), 25, 915–920, 2000.

Mittermaier M. P. and Illingworth, A. J.: Comparison of model-derived and radar-observed freezing-level heights: implications for vertical reflectivity profile-correction schemes, Q. J. Roy. Meteorol. Soc., 129, 83–95, 2003.

Ozturk, K. and Yilmazer, A. U.: Improving the accuracy of the radar rainfall estimates using gage adjustment techniques: Case study for west Anatolia, Turkey, Atmos. Res., 86, 139–148, 2007.

Peebles, J. P. Z.: Radar principles, Wiley-Interscience, New York, USA, 1998.

Pruppacher, R. and Beard, K. V.: A wind tunnel investigation of the internal circulation and shape of water drops falling at terminal velocity in air, Q. J. Roy. Meteor. Soc., 96, 247–256, 1970.

Russo, F., Napolitano, F., and Gorgucci, E.: Rainfall monitoring systems over an urban area: the city of Rome, Hydrol. Process., 19, 1007–1019, 2005.

Russo, F., Lombardo, F., Napolitano, F., and Gorgucci, E.: Rainfall stochastic modelling for runoff forecasting, Phys. Chem. Earth, 31, 1252–1261, 2006.

Saltikoff, E., Koistinen, J., and Hohti, H.: Experience of real time spatial adjustment of the Z-R relation according to water phase of hydrometeors, Phys. Chem. Earth, 25, 1017–1020, 2000.

Seo, D. J., Breidenbach, J., Fulton R., O'Bannon, T., and Miller D.: Real-time adjustment of range-dependent biases in WSR-88D rainfall estimates due to nonuniform vertical profile of reflectivity, J. Hydrometeorol., 1, 222–240, 2000.

Serinaldi, F.: Analysis of inter-gauge dependence by Kendall's τ_K, upper tail dependence coefficient, and 2-copulas with application to rainfall fields, Stoch. Env. Res. Risk A., 22, 671–688, 2008.

Steiner, M., Houze, J. R. A., and Yuter, S. E.: Climatological characterization of three-dimensional storm structure from operational radar and rain gauge data, J. Appl. Meteorol., 34, 1978–2007, 1995.

Vignal, B. and Krajewski, W. F.: Large-sample evaluation of two methods to correct range-dependent error for WSR-88D rainfall estimates, J. Hydrometeorol., 2, 490–504, 2001.

Vignal, B., Galli, G., Joss, J., and Germann, U.: Three methods to determine profiles of reflectivity from volumetric radar data to correct precipitation estimates, J. Appl. Meteorol., 39, 1715–1726, 2000.

Villarini, G. and Krajewski, W. F.: Review of the different sources of uncertainty in single polarization radar-based estimates of rainfall, Surv. Geophys., 31, 107–129, 2010.

Villarini, G., Mandapaka, P. V., Krajewski, W. F., and Moore, R. J.: Rainfall and sampling uncertainties: A rain gauge perspective, J. Geophys. Res., 113, D11102, doi:10.1029/2007JD009214, 2008a.

Villarini, G., Serinaldi, F., and Krajewski, W. F.: Modeling radar-rainfall estimation uncertainties using parametric and non-parametric approaches, Adv. Water Resour., 31, 1674–1686, 2008b.

Vulpiani, G., Montopoli, M., Delli Passeri, L., Gioia, A. G., Giordano, P., and Marzano, F. S.: On the use of dual-polarized C-band radar for operational rainfall retrieval in mountainous areas, J. Appl. Meteor. Climatol., 51, 405–425, 2012.

Wang, Y. and Chandrasekar, V.: Quantitative precipitation estimation in the CASA X-band dual-polarization radar network, J. Atmos. Ocean. Tech., 27, 1665–1676, 2010.

Yoo, C. and Ha, E.: Effect of zero measurements on the spatial correlation structure of rainfall, Stoch. Env. Res. Risk. A., 21, 287–297, 2007.

Yuter, S. E. and Houze, J. R. A.: Three-dimensional kinematic and microphysical evolution of Florida cumulonimbus. Part I: spatial distribution of updrafts, downdraft and precipitation, Mon. Weather Rev., 123, 1921–1940, 1994.

Zawadzki, I.: Factors affecting the precision of radar measurements of rain, in: Proceeding of the 22d Conf. Radar Meteorology, Zurich, Switzerland, 10–13 September 1984, Amer. Meteor. Soc., 251–256, 1984.

Zhang, J. and Qi, Y.: A real-time algorithm for the correction of brightband effects in radar-derived QPE, J. Hydrometeorol., 11, 1157–1171, 2010.

Zhang, J., Langston, C., and Howard, K.: Brightband identification based on vertical profiles of reflectivity from the WSR-88D, J. Atmos. Ocean. Tech., 25, 1859–1872, 2008.